JOURNAL OF QUATERNARY SCIENCE (2021) 1–12 ISSN 0267-8179. DOI: 10.1002/jqs.3314

JQS Journal of Quaternary Science QRA Quaternary Research Association

Volcanic ash and tsunami record of the Minoan Late Bronze Age Eruption (Santorini) in a distal setting, southwestern Turkey

ERKAN AYDAR,[1]* ATTILA ÇİNER,[2] ORKUN ERSOY,[1] EMILIE ÉCOCHARD[3] and ERIC G. FOUACHE[3]
[1]Department of Geological Engineering, Hacettepe University, Ankara, Turkey
[2]Eurasia Institute of Earth Sciences, Istanbul Technical University, Istanbul, Turkey
[3]Department of Geography, Paris Sorbonne IV University, Paris, France

Received 13 July 2020; Revised 21 March 2021; Accepted 23 March 2021

ABSTRACT: We present the volcanic ash and tsunami record of the Minoan Late Bronze Age Eruption of Santorini (LBAES) in a distal setting in southwestern Turkey. In one of the drilled cores at the Letoon Hellenic antique site on Eşençay Delta, we encountered a 4 cm thick tephra deposit underlain by 46 cm thick tsunami-deposited sand (tsunamite), and an organic-rich layer that we ^{14}C dated to 3295 ± 30 BP or 1633 BC. The relationship between Santorini distal volcanic ash and underlying tsunamite is described and interpreted. LBAES occurred in four main phases: (1) plinian; (2) phreatomagmatic; (3) phreatomagmatic with mudflows; and (4) ignimbritic flows and co-ignimbrite tephra falls. In this study, we aim to understand which eruptive phases generate distal ash during the Minoan eruptive sequence by examining the 3D surface morphology of ash formed by different fragmentation processes. To that end, we used numerous statistical multivariates, 3D fractal dimension of roughness, and a new textural parameter of surface area-3D/plotted area-2D to characterise the eruption dynamics. Based on ash surface morphologies and the calculated statistical parameters, we propose that that distal ash is represented by a single layer composed of well-mixed (coarse to fine) magmatic and phreatomagmatic ash.

KEYWORDS: 3D ash analysis; distal ash; Minoan eruption; polyhedron ash; Santorini; SA/PA; tsunami; Turkey

Introduction

Volcanic ash injected into the atmosphere during an explosive eruption can be transported far in distal (>100 km) and ultradistal (up to thousands of kilometres) regions by winds. Correlating back to their volcanic source allows tephrochronological studies to provide information on the eruption frequency and geochemical evolution of volcanic regions and individual volcanoes (Abbott *et al.*, 2020). More information is needed on volcanic eruptions, especially the morphology of volcanic ash that is an indicator for volcanic ash types indicating the magmatic fragmentation style, eruption dynamics, etc. The particle and vesicle shapes, ash surface properties, ash types and pumice texture preserve details on the eruption dynamics that produced them. Furthermore, volcanic ash particle shapes and surface properties are essential to understanding the intensity of eruption (Bonadonna *et al.*, 1998). The surface texture and morphologies of volcanic ash particles change according to various fragmentation mechanisms (Heiken and Wohletz, 1985; Wohletz, 1983; Dellino and La Volpe, 1996; Dellino and Liotino, 2002; Ersoy *et al.*, 2006, 2007; Cioni *et al.*, 2008, Liu *et al.*, 2015). The common shapes of glass pyroclasts in phreatomagmatic eruptions can be ascribed to varying energies and modes of contact of water with magma, including blocky-equant, moss-like, plate-like and drop or spherical (Wohletz, 1983). They also represent planar–curviplanar surfaces that may cut vesicle walls. In general, those glass shards are blocky in shape, low in vesicularity, and have a low-to-moderate microlite content (Nemeth, 2010). In contrast, a plinian eruption produces vesicularities that can reach 75–85% in pumice clasts (Klug *et al.*, 2002). The pumices can contain micro-, tubular, coalesced and/or expanded vesicles as a function of the fragmentation processes (Polacci *et al.*, 2003). Additionally, Wohletz (1983) states that magmatic fragmentation leads to the formation of some tubular, elongate, spherically vesiculated fragments. The quantitative characterisation of ash particle morphology and texture helps to identify eruption dynamics (Dellino and La Volpe, 1996; Dellino and Liotino, 2002; Ersoy *et al.*, 2006, 2007; Cioni *et al.*, 2008, Liu *et al.*, 2015).

This study's location is in the Eşençay Delta near the Letoon Hellenic antique site, classified under the UNESCO World Heritage List since 1988, in the southwest of Turkey *c.* 350 km east of Santorini (Fig. 1). In one of the drilled cores, we encountered a 4 cm thick tephra deposit underlain by 46 cm thick tsunami-deposited sand (tsunamite). Thus, we infer that those deposits relate to the Late Bronze Age Eruption of Santorini (LBAES) based on the sedimentological features of the sand level and the presence of isochronous organic level with the LBAES eruption and overlying LBAES tephra deposit and comparison of the similar stratigraphic position with the tsunamites in neighbouring sectors in the Eastern Mediterranean. The LBAES shows very complexly varying eruption dynamics within a single eruptive sequence, from dry plinian to phreatomagmatic explosions, and ignimbritic flows and their associated co-ignimbrite tephra falls (Druitt *et al.*, 2019; a summary of the LBAES is provided below, with the relevant significant references). Volcanic ash of the LBAES has been deposited either as marine tephra in the Aegean, Mediterranean and Black Seas or as terrestrial tephra in the Aegean islands or mostly in Turkey (Druitt *et al.*, 2019). Except for Sparks *et al.* (1983), there is no other detailed study on the entire eruptive phases or dynamics produced by LBAES distal ash.

The LBAES explosion also created a tsunami, of which records are found throughout the Mediterranean basin (Minoura *et al.*, 2000; Goodman-Tchernov *et al.*, 2009). It is

*Correspondence: E. Aydar, as above.
E-mail: eaydar@hacettepe.edu.tr

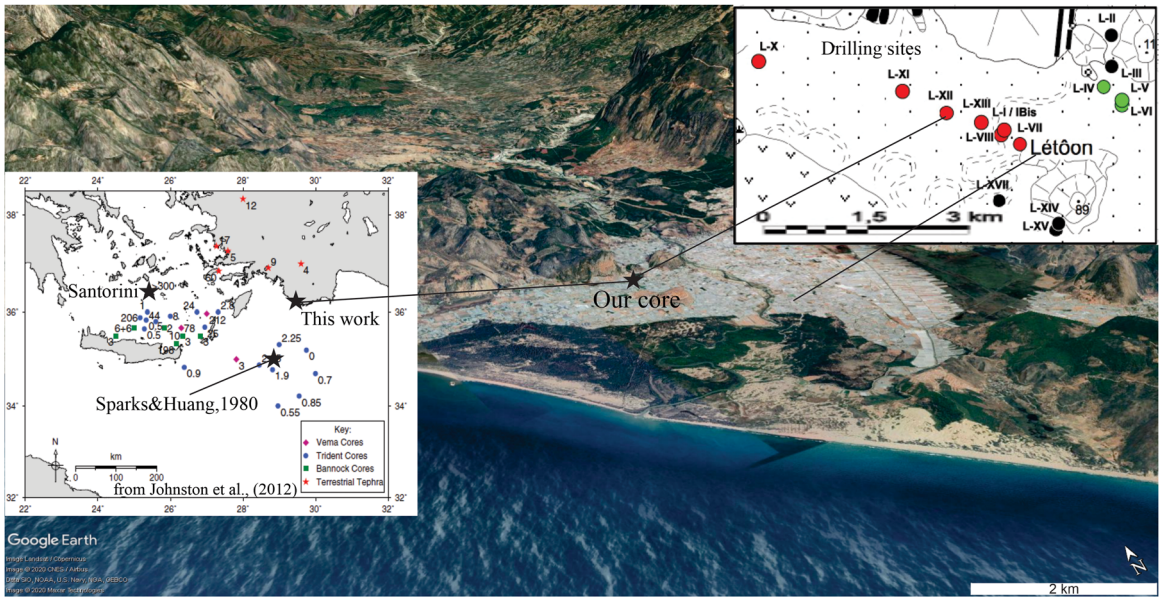

Figure 1. Locations of Santorini and Letoon Sanctuary, with the location of the L-XII core. Stars correspond to Letoon and a marine core described by Sparks and Huang (1980). Small sketch by Johnston *et al.* (2012) exhibits all marine and terrestrial exposures of LBAES tephra. [Color figure can be viewed at wileyonlinelibrary.com].

estimated that around 5% of tsunamis were caused by volcanic eruptions (Smith and Shepherd, 1995). However, tsunamites in the geological record are difficult to identify as they often contain several facies that can be attributed to other processes (e.g. storm deposits) and hence need to be described with utmost care (e.g. Dawson and Steward, 2007; Peters and Jaffe, 2010).

In this study, we focus on two deposits related to the LBAES. First, we explain the origin of the sand immediately underneath the ash layer and its relationship with the tsunami that originated from the LBAES eruptive cycle. Secondly, we examine the morphological and volcanological properties of ash in the LBAES distal tephra to interpret which eruptive phases they belong to. Besides the conventional correlating methods (chemistry, grain size, etc.), we also apply some relatively new techniques, based on scanning electron microscopy imaging and statistical calculations (fractal dimension roughness, surface morphology parameters, etc.), to characterise distal tephra deposits and related eruption dynamics. We also used Acıgöl phreatomagmatic (eruption U/Th-He age dated to 20.3 ± 0.6 ka by Schmitt *et al.*, 2011), and Dikkartın plinian tephra (eruption characteristics described in Ersoy *et al.*, 2019) (^{36}Cl cosmogenic surface exposure dated to 7.6 ± 0.6 ka by Sarıkaya *et al.*, 2019, and U/Th-He dated to 9.03 ± 0.55 ka by Friedrichs *et al.*, 2020) as two well-known proxies to compare with the LBAES distal ash.

Methodology

Drilling

We drilled a total of 10 sites in the Eşençay Delta by using a geoprobe truck that works with a direct push technique causing little or no disturbance to the cores. In the lower parts of the longest core (core L-XII; UTM, 704520 N/4023652 E), *c.* 9.5 m in length, we encountered the volcanic ash and tsunamite layers (Fig. 2).

Scanning electron microscope analyses

Scanning electron microscope (SEM) analyses of the sediments helped to identify the mineralogy and the grain size and qualify roundness and shape. We reported microprobe analyses of glassy tephra to define the chemistry of the volcanic ash performed at Pisa University, Italy, using a EDAX-DX detector of Philips SEM 515 with operating conditions of 20 kV acceleration voltage, 5 nA beam current, 100 s live time counting, 200–500 nm beam diameter, and ZAF correction.

To evaluate the tephra's surface texture, we applied numerous 3D analyses (about 110 ash members' details are given in the supporting information) on randomly sampled volcanic ash using ZEISS EVO-50 SEM at Hacettepe University in Ankara, Turkey. Alicona-MeX 5.1. software was used to obtain the 3D images.

The outline of ash grains on constituted 3D images was drawn as a polygon, and later, all textural descriptors such as roughness parameters, surface area, projected area, volume, the fractal dimension of surface (DSA), profile analyses and all statistical surface parameters were calculated, conforming to the International Standards of EN ISO 4287/4288. All these parameters and profiles are illustrated in the supporting information. This method was previously applied to volcanic ash and detailed by Ersoy (2010).

Grain-size analysis

The grain-size distribution was calculated using a Sympatec Laser Sizer H-1305 that works with laser diffraction. The accuracy of the analysis was observed by performing analyses in triplicate. The grain size was further calculated by wet-sieving down to 63 µm. The method is entirely built to the specifications of ISO 13320 *Particle size analysis-laser diffraction methods* and designed for absolute precision measurements to typically ± 1% deviation concerning the standards. H-1305 is a very high precision sensor of HELOS (Helium-Neon-Laser Optical System; https://www.sympatec.com).

^{14}C dating

The sample taken from the organic level immediately beneath the ash was analysed for ^{14}C dating at the Centre of Radiocarbon Dating, University Claude Bernard Lyon1, France. The age determination made with the accelerator

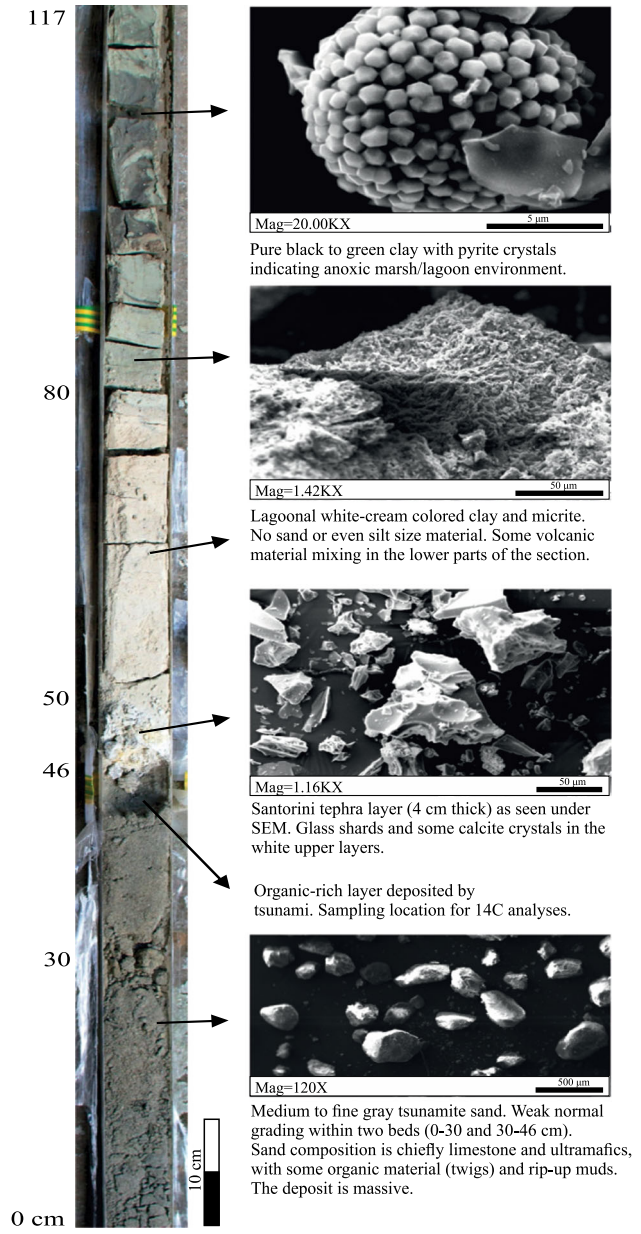

Figure 2. Description and interpretation of 117 cm long core derived from the L-XII drilling near the Letoon Sanctuary in southwestern Turkey. [Color figure can be viewed at wileyonlinelibrary.com].

mass spectrometry (AMS) method was calibrated, catalogued in the laboratory with the number Lyon7920, and the result was reported to us.

Brief outlines of the minoan eruption

The Minoan civilisation was severely hit by the pyroclasts and the tsunami generated by the powerful and catastrophic explosive eruption of the Santorini Volcano in the Aegean Sea (Minoura *et al.*, 2000; Athanassas *et al.*, 2017). This LBAES (also known as the Minoan Eruption of Santorini) occurred at *c.* 1600 BC (1600–1627 BC, Friedrich *et al.*, 2006; 1613 ± 13 BC, Friedrich, 2013) and produced an enormous volume of tephra (78–86 km^3 DRE, Johnston *et al.*, 2014). Precursory phreatic and phreatomagmatic eruptions covered Thera Island in 4 cm (Heiken and McCoy, 1984) to 9 cm of thick fine ash (Druitt *et al.*, 2019). The volcanic stratigraphy includes four main phases (Bond and Sparks, 1976; Heiken and McCoy, 1984; Sigurdsson *et al.*, 1990; Druitt *et al.*, 1999, 2019; Friedrich *et al.*, 2006; McCoy and Heiken, 2000; Taddeucci and Wohletz, 2001; Druitt, 2014; Nomikou *et al.*, 2016; Druitt *et al.*, 2019): (1) plinian; (2) phreatomagmatic with thick cross-bedded fine-grained ash layers, interbedded fall layers; (3) phreatomagmatic (compound) with chaotic, unsorted mudflows and base surge deposits; and (4) pyroclastic flows and related co-ignimbrite tephra falls.

The associated tephra layers were mainly found in marine cores in the Mediterranean Sea (Sparks and Huang, 1980; Sparks *et al.*, 1983; Wulf *et al.*, 2002; Aksu *et al.*, 2008; Hamann *et al.*, 2010; Satow *et al.*, 2015), in the Black Sea (Guichard *et al.*, 1993; Cullen *et al.*, 2014) and as terrestrial tephra in Turkey, Egypt, Israel and on several Greek islands (Stanley and Sheng, 1986; Sullivan, 1990; Öner, 1996; Roberts *et al.*, 1997; Eastwood *et al.*, 1999, 2002; Écochard *et al.*, 2009; Sulpizio *et al.*, 2013; Öner, 2019).

Toward the end of the eruptive sequence, the catastrophic tsunami waves were generated by the pyroclastic flows of phases 3 and 4 entering the sea (Nomikou *et al.*, 2016; Druitt *et al.*, 2019).

The outline of the voluminous tephra of the entire Minoan eruption, drawn by McCoy and Heiken (2000), represents an envelope of *c.* 1500 km crosswind (from the Nile Delta to the Black Sea), >2000 km downwind (from Santorini to eastern Turkey) in east-southeast-northeast directions. McCoy and Heiken (2000) also noticed that tropospheric winds transported LBAES tephra at lower elevations to the east and east-southeast, and at higher elevations by stratospheric winds (jet stream) that changed direction from the east over the southern Aegean Sea to the north and northeast over Anatolia and the Black Sea.

Results

Core description

Among the 10 drilled cores from the Eşençay Delta, volcanic ash and tsunamites were encountered only in core L-XII; today situated *c.* 4.5 km from the actual shoreline. Although the total length of the core is 9.5 m, in this study, we describe only the basal undisturbed 117 cm, on which we carried out detailed sedimentological and mineralogical studies (Fig. 2).

Between 0 and 46 cm, medium- to fine-grained grey sand is present. The sand grains are rounded to well-rounded, indicating a coastal/nearshore source. Additionally, this sand contains few marine bivalves (*Cerastoderma glaucum*) and gastropods (*Potamides conicus*) (Écochard *et al.*, 2009) that were probably transported together with the sand grains to their final depositional setting. No ash was found at this level.

The sandy layer is possibly made of two separate layers. In the lower layer (0–30 cm), grain size slightly decreases upwards, and a few thin tree branches in a vertical position are found, together with a rip-up mud clast that is disseminated within the sand. No sedimentary structures are observed. The upper layer (30–46 cm) is similar in composition and shows a slight fining upward tendency with a sharp lower contact. The uppermost part (43–46 cm) is very rich in organic debris, which enabled material to be collected for ^{14}C dating (3295 ± 30 BP or 1633 BC, calibrated age; AMS method-Lyon7920). This age perfectly matches previously dated LBAES by Friedrich *et al.* (2006) and Friedrich (2013).

A 4 cm thick layer of tephra (46–50 cm) directly overlies this organic-rich layer. The tephra layer is massive and shows no internal structures. The grain-size distribution and composition

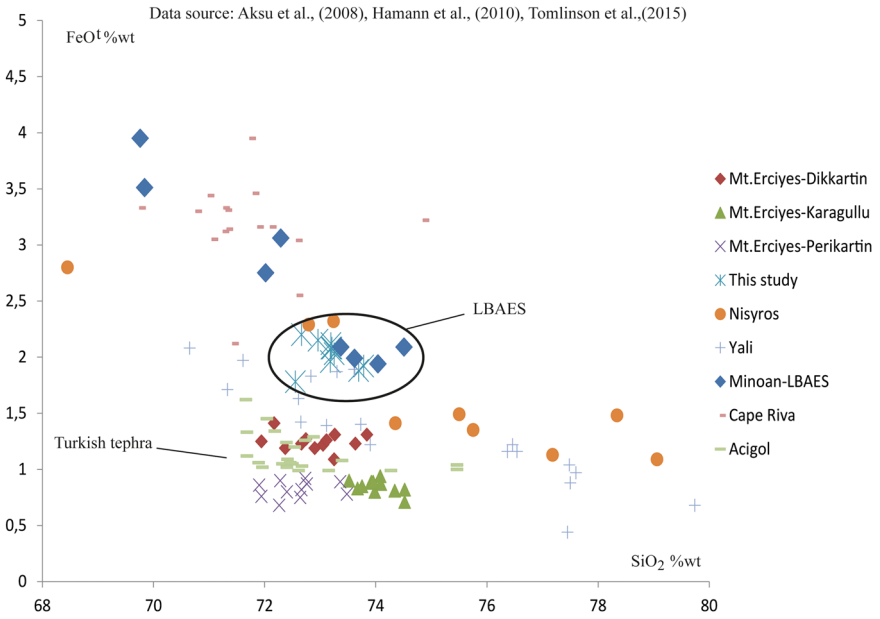

Figure 3. Chemistry of volcanic glass from Santorini, Dodecanese Province and Turkish volcanoes. Our microprobe analyses of glassy tephra were performed at Pisa University, Italy, using an EDAX-DX detector of Philips SEM 515. Other chemical analyses were compiled from Aksu *et al.* (2008), Hamann *et al.* (2010) and Tomlinson *et al.* (2015) and references therein. [Color figure can be viewed at wileyonlinelibrary.com].

of this yellowish-white, fine-grained layer are explained in more detail in the following sections.

A white–cream-coloured $CaCO_3$-bearing homogeneous mudstone interval (50–80 cm) overlies the tephra deposit. The ash's basal part has a sharp contact, while the transition from ash to the upper mudstone is gradational with the mudstone layer above. SEM analysis shows that the gradational zone is made of clay and calcite minerals and volcanic glass shards. Glass shards disappear towards this unit's upper parts, made of black to green-coloured pure mudstone (80–117 cm). The colour becomes darker up-section, and some pyrite crystals are found scattered throughout the clay minerals (Fig. 2).

Description and characterisation of the volcanic ash

Chemistry

We performed a series of major-element glass chemical analyses on our tephra deposits. The FeOt-SiO_2 discrimination diagram was used to compare the available published analyses with those obtained in this study (Fig. 3). Glass chemistry of our tephra indicates that the magma erupted was rhyolitic with its average SiO_2 close to 73 wt% (Table 1). In addition to the ^{14}C age, this glass matches very well with LBAES tephra with its high iron content (≥2 wt%) and is distinct from Turkish (in general <2 wt %) and some other Cycladic tephras (Fig. 3).

Grain size and composition

The components of our tephra are illustrated in a back-scattered electron image of SEM (Fig. 4). It is composed of pumice grains (up to 400 μm), glass shards, dense lava fragments and individual minerals. Our laser sizer equipment measurements show that the tephra is mostly fine-grained, as expected from distal ash, although the coarsest fragments reach *c.* 400 μm (Table 2). Laser sizer yields *c.* 2.73% for + 300 μm fraction for dry measurement, and this was checked via conventional screening and obtained 3.57% for + 300 μm fraction. Our tephra's grain-size distribution is unimodal (Fig. 5) and contains fragments 62% coarser than 4 phi.

Surface texture and morphology

We compared quantitative morphological data acquired for <63 and <125 μm grain-sized tephra from LBAES with the same grain size of the well-known eruptions of Dikkartın plinian deposits (DPD) from central Turkey (for details of the

Table 1. Glass chemistry of tephra found at Letoon. Chemical analyses were performed by Philips SEM 515-EDAX with accelerating voltage: 15 kV; counting time: 100 s; and ZAF corrections reported

PI-115 L-XII	SiO_2	TiO_2	Al_2O_3	FeOtot	MnO	MgO	CaO	Na_2O	K_2O	P_2O_5	ClO	Total
PI-115-1	73.69	0.20	14.21	1.88	0.00	0.38	1.14	4.85	3.34	0.00	0.31	100.00
PI-115-2	73.18	0.27	14.41	1.96	0.00	0.45	1.39	4.88	3.18	0.00	0.29	100.01
PI-115-3	73.25	0.26	14.32	2.03	0.00	0.35	1.44	4.55	3.55	0.00	0.23	99.98
PI-115-4	72.96	0.36	14.37	2.15	0.15	0.26	1.53	4.73	3.30	0.00	0.19	100.00
PI-115-5	72.66	0.31	14.58	2.20	0.12	0.45	1.41	4.78	3.25	0.00	0.23	99.99
PI-115-6	73.19	0.25	14.31	2.08	0.00	0.28	1.39	5.01	3.21	0.00	0.29	100.01
PI-115-7	73.21	0.35	14.41	2.08	0.19	0.32	1.60	4.42	3.28	0.00	0.14	100.00
PI-115-8	73.78	0.35	14.15	1.92	0.00	0.20	1.20	4.85	3.38	0.00	0.19	100.02
PI-115-9	72.55	0.28	14.76	1.78	0.00	0.33	1.66	5.17	3.24	0.00	0.23	100.00
PI-115-10	73.19	0.32	14.19	2.12	0.06	0.30	1.45	4.66	3.40	0.00	0.30	99.99
Average	**73.17**	**0.30**	**14.37**	**2.02**	**0.05**	**0.33**	**1.42**	**4.79**	**3.31**	**0.00**	**0.24**	-
Standard deviation	**0.39**	**0.05**	**0.19**	**0.13**	**0.07**	**0.08**	**0.16**	**0.22**	**0.11**	**0.00**	**0.06**	-

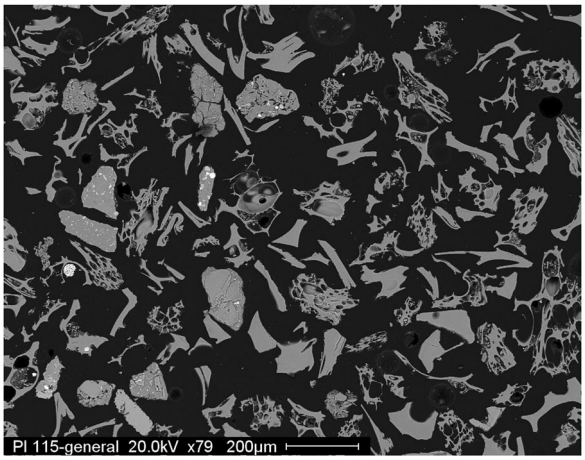

Figure 4. Back-scattered electron image of our tephra.

eruption see Şen *et al.*, 2002 and Ersoy *et al.*, 2019) found as Mediterranean marine tephra off the coast of Israel (Hamann *et al.*, 2010) and rhyolitic phreatomagmatic deposits from the Acıgöl Rhyolitic Maar Crater (ARM), in central Turkey. Although it is not ideal to compare proximal ash from Acıgöl and Dikkartın with the distal marine ash of the LBAES, these ashes were used as thresholds for phreatomagmatic and plinian fragmentations. The glassy ash of DPD has mostly elongate, tubular vesicles (Fig. 6), even though during the early phases of this eruption there is some evidence for significant phreatomagmatism (Şen *et al.*, 2002; Ersoy *et al.*, 2019).

Table 2. Grain-size analysis by laser sizer

Particle size (µm)	Tephra (% cumulative)
435	100
365	98.98
305	97.5
255	95.21
215	92.66
180	89.92
150	86.58
125	82.48
105	77.45
90	72.52
75	66.53
62.5	60.29
52.5	54.39
45	49.64
37.5	44.49
30	38.24
25	33.17
21.5	29.32
18.5	26
15.5	22.82
13	20.33
11	18.39
9	16.39
7.5	14.7
6.5	13.39
5.5	11.88
4.5	10.11
3.6	9.5
3	8.53
2.6	7.31
2.2	6.04
1.8	4.72

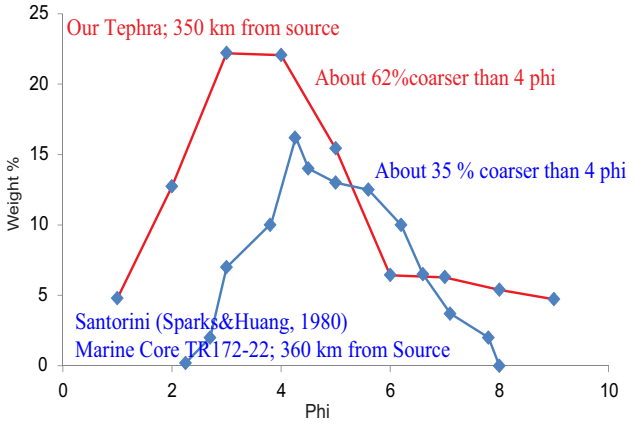

Figure 5. A comparison of the grain-size distribution of our tephra (red) with marine core tephra (blue) of Santorini (data source Sparks and Huang, 1980) at a similar distance. [Color figure can be viewed at wileyonlinelibrary.com].

Additionally, the tephra from ARM is mainly blocky-equant, plate-like and sometimes exhibits curviplanar vesicles (Fig. 6).

On the other hand, our LBAES tephra's fragments have either tubular, spherical vesicles indicating magmatic fragmentation, or they are sometimes blocky-equant, moss-like grains and curviplanar cut and shallow vesicles depicting typical phreatomagmatic fragmentation (Fig. 7). The 3D surface roughness of the LBAES tephra fluctuates between nanoscale and micron-scale asperities.

A polyhedron type of unvesiculated ash exists within the tephra together with blocky-equant ash. The irregular geometry due to multifractal features and faces give some spikes on roughness profiles. Roughness profiles of blocky distal ash from the LBAES are more regular than ARM base surge deposits (Fig. 6). Further, the surfaces of the ash from DPD have micron-scale fluctuations, differing from phreatomagmatic blocky ash (Figs. 6 and 7).

Fractal dimension of surface of volcanic ash

The 3D fractal dimension of surface roughness shows that the fractal dimension values of DPD are higher than 2.06, with an average of 2.083 ($2.063 < DSA < 2.101$) (see supporting information). Besides, ARM phreatomagmatic deposits are mostly less than 2.04, with an average of 2.032 ($2.020 < DSA < 2.047$) (Fig. 6). LBAES distal tephra is investigated in two grain-size fractions: <125 µm and <63 µm. The coarser tephra grains have fractal dimension values between ARM and DPD with 2.046 on average ($2.022 < DSA < 2065$). Conversely, the fractal dimension values of the finer grain size (<63 µm) of LBAES distal tephra are as high as DPD deposits with an average of >2.06 ($2.044 < DSA < 2.11$), due to abundant unvesiculated polyhedron ash and abundant crushed pumices.

Surface area vs. volume of ash members

The surface area–volume ratio (SA/V) of ash changes according to the investigated grain size. Therefore, different grain-size fractions of LBAES distal tephra deviate on related diagrams (Fig. 7 and supporting information). In <63 µm size fractions, the average SA/V of DPD fall deposits is *c.* 0.15, while ARM base surge ash gives an average of 0.1841. With those proxies, LBAES <125 µm sized ash is comparable with DPD falls, having an SA/V equal to 0.146 on average. On the other hand, LBAES <63 µm deposits have conspicuously very high average

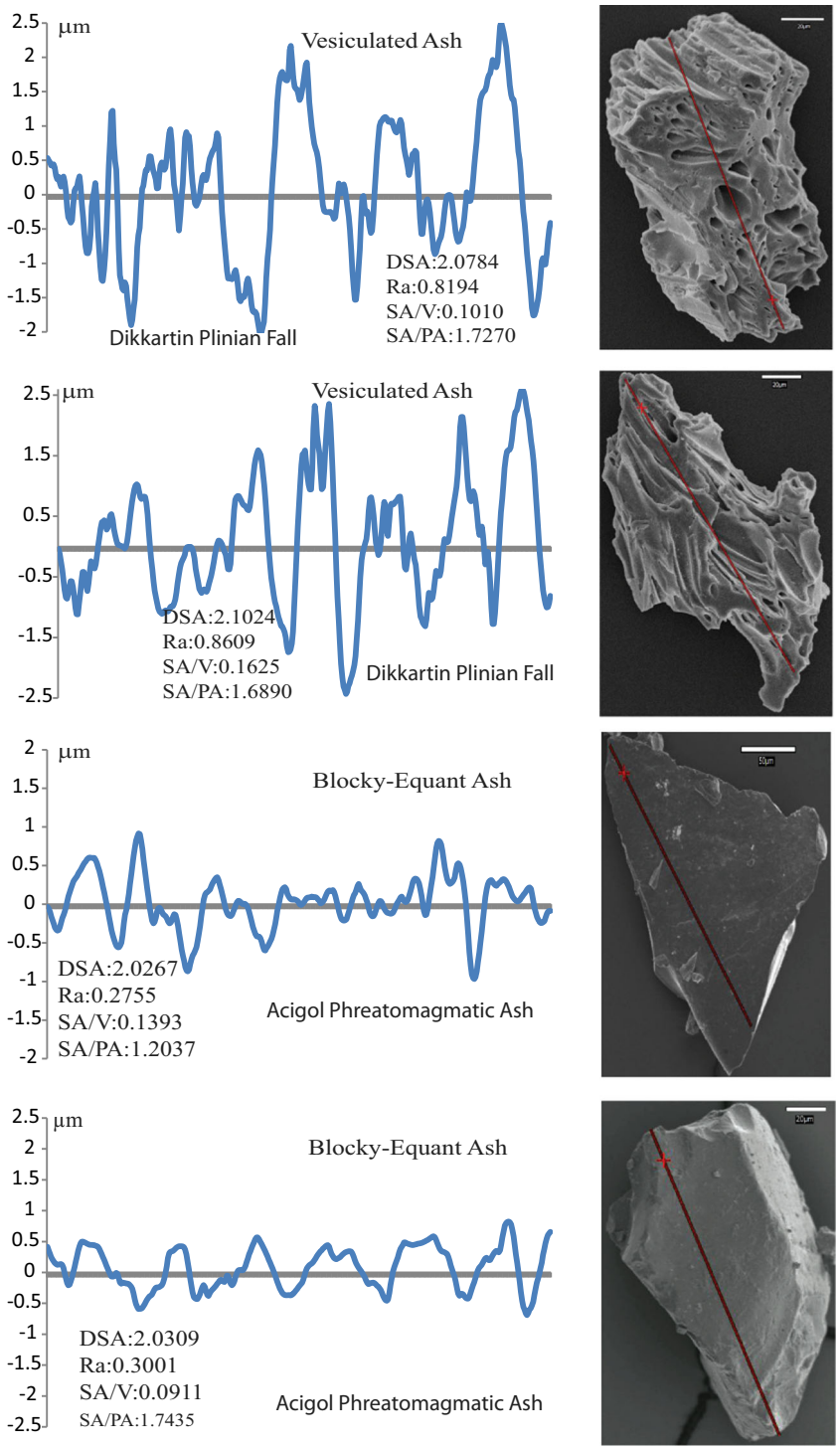

Figure 6. Surface roughness profiles of Dikkartın and Acıgöl tephras with 3D SEM image and calculated textural descriptors. Nano-scaled variations on glassy ash exhibit mostly quenching event. Meanwhile, more irregular profiles are attributed to vesiculation due to magmatic fragmentation as also shown in Fig. 7. [Color figure can be viewed at wileyonlinelibrary.com].

SA/V values (0.459), where polyhedron ash and crushed pumices dominate.

Surface area vs. projected area

We also calculated the 'true surface area (SA) and projected area (PA)' of ash members (Figs. 8 and 9; supporting information). As SA is computed on the 3D image, PA corresponds to a 2D projection. SA/PA values of LBAES <63 µm deposits vary from 1.35 to 3.96, while those of 125 µm range between 1.32 and 2.18. Comparing all SA/PA values, we conclude that the vesiculated ash (dry-magmatic) has an SA/PA of *c.* 1.8 and over, the polyhedron-multifractal, unvesiculated glassy ash has SA/PA values >2, while blocky-equant ash has SA/PA values <1.6 (supporting information).

Discussion

Plinian vs. co-ignimbrite falls: ash dispersal aspect

The paroxysmal plinian eruption of LBAES is followed by phreatomagmatic phases (phases 2 and 3) with occasional pyroclastic flows. Finally, multiflow units of ignimbrites and related co-ignimbrite ash falls were emplaced and found as

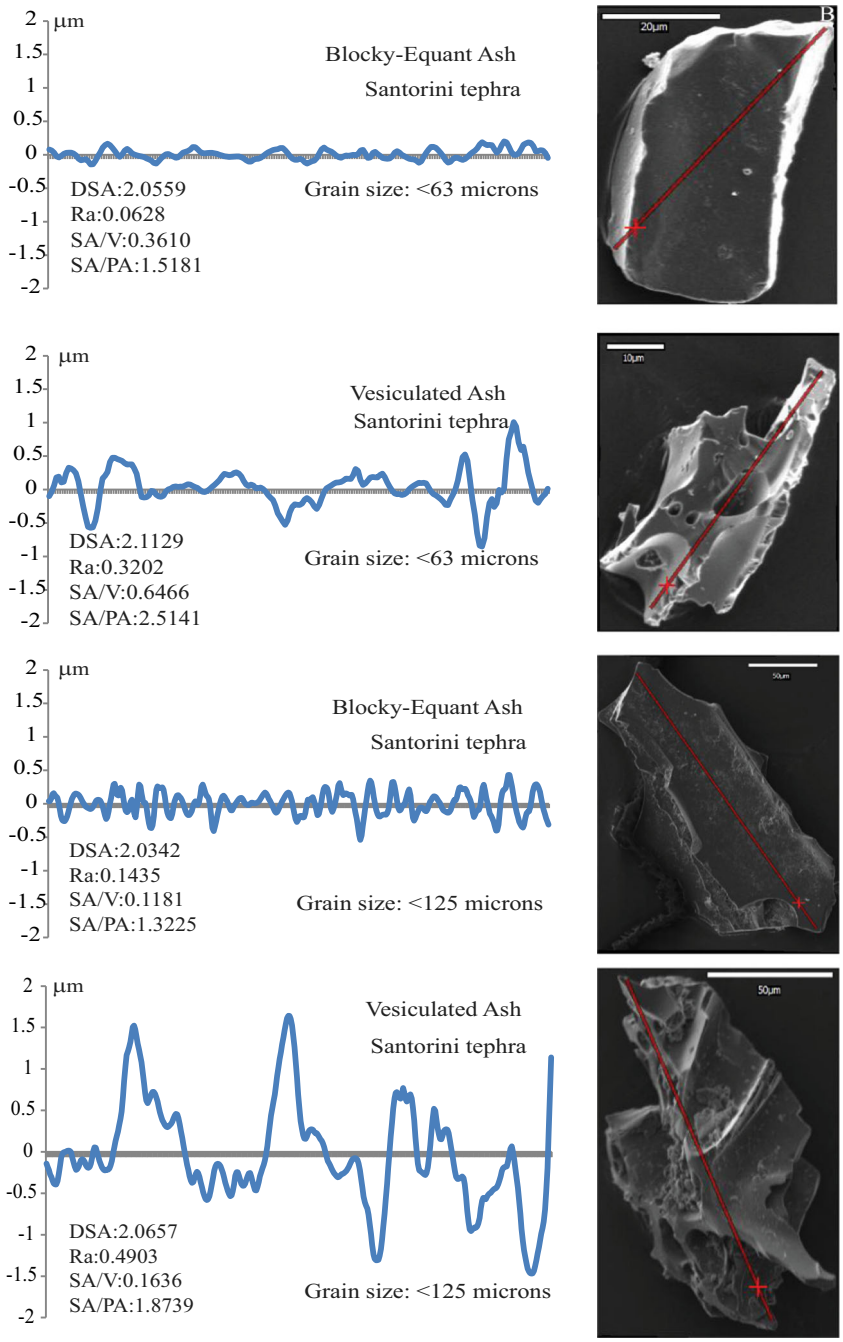

Figure 7. Surface roughness profiles of the Santorini tephra with 3D SEM image and calculated textural descriptors. [Color figure can be viewed at wileyonlinelibrary.com].

marine tephra (Sparks and Huang, 1980; Sparks *et al.*, 1983). Engwell *et al.* (2014) claimed that the coarse plinian fall deposits and overlying finer co-ignimbrite falls were deposited as two separate layers at *c.* 130 km from the source area. The distal facies (between 400 and 1000 km from the source area) cannot be divided into separate units and show distinct grain-size bimodality. However, Sparks and Huang (1980) quote that >90% of distal ash is related to co-ignimbrite falls.

Sparks and Huang (1980) performed detailed grain-size analysis on LBAES tephra deposits from marine cores. They concluded that grain size has a bimodal distribution where the coarser size corresponds to plinian fall deposits. In contrast, finer ones exhibit a co-ignimbrite origin in cores closer to the source area. Moreover, Sparks and Huang (1980) note that the grain-size distribution of tephra from the marine core becomes unimodal 330 km away from the source area with a very fine grain-size population (<4 phi), representing only co-ignimbrite vitric fine ash, which provided the majority of the distal material of LBAES.

We compared our LBAES distal tephra with Sparks and Huang's (1980) results on marine core tephra of a similar distance from Santorini (350 km and 360 km, respectively, located on Fig. 1) (Fig. 5). Our pumices reach 400 µm in size, and the deposits also contain dense lithics and free crystals. The grain-size distribution of our tephra is unimodal, as also claimed by Sparks and Huang (1980). Furthermore, 62% of our tephra is coarser than 4 phi, in contrast to what Sparks and Huang (1980) found in marine tephra from a similar distance, although the grain-size distribution by distance is under wind control, which has a crucial effect on the plume. However, we can say that the difference in grain-size distribution shows that our tephras are more heterogeneous than marine tephras.

The LBAES distal ash constitutes a key horizon along Eşençay River with a constant thickness *c.* 5–10 cm, encountered a few

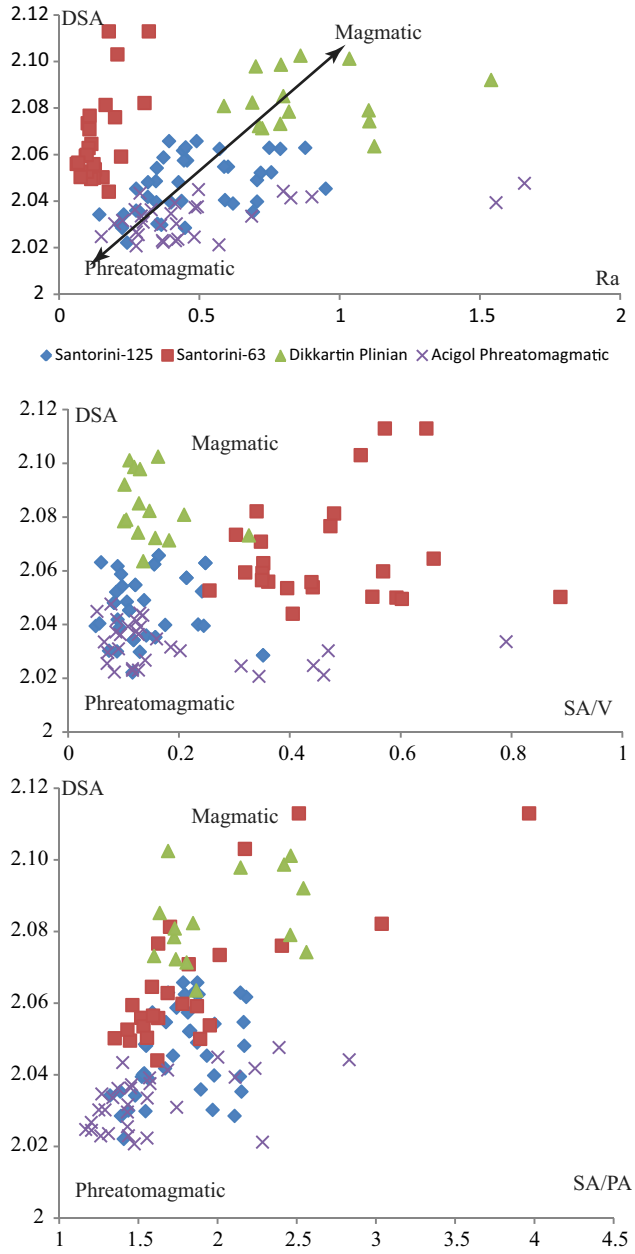

Figure 8. Bivariate correlation diagrams of calculated textural parameters of all tephra used. DSA: fractal dimension of the profile; Ra: average roughness of profile; SA: surface area; PA: projected area; V: volume. All statistical parameters are available upon request. [Color figure can be viewed at wileyonlinelibrary.com].

metres below the present sea level (Öner, 1996, 2019). Based on this observation, we propose that the studied tephra, which shows no internal stratifications attributable to any reworking processes related to wind or current activity, is in place and constitutes a continuous layer toward inland.

3D quantification of surface parameters and ash morphology

To quantify the shape parameters, the fractal and the multifractal dimension of volcanic ash particles' contours were investigated in 2D by Dellino and Liotino (2002) and Nurfiani and Bouvet de Maisonneuve (2018). Measurement of two-dimensional parameters on particles' outlines is easier and faster but less reliable (Ersoy, 2010). However, the 3D surface morphology studies of the volcanic ash are less well known. Since volcanic ash may present very complex shapes and surface features in the 3D view, we discuss this topic.

Volcanic particle morphology can help discriminate between clasts formed in different volcanic environments and produced by other eruptive mechanisms. The 2D fractal dimension of volcanic ash particle contour work of Dellino and Liotino (2002) suggests that phreatomagmatic particles present monofractals, whereas magmatic particles exhibit multifractal properties due to abundant ruptured vesicles. Their contour may be correlated with our PA outline (Fig. 9).

Our 3D work on LBAES tephra allowed us to define 'polyhedron ash', which is an unvesiculated vitric volcanic ash, described here for the first time (Fig. 10). This polyhedron ash shows highly brittle aspects and is not as equant as blocky-equant ash. It can be pyramidal or present irregular angular shapes. Polyhedral elements of an ash surface may be related to extreme and intensive brittle fracturing of the melt as defined by Büttner *et al.* (2002). The hydrovolcanic fragmentation mechanism involves a form of brittle fracture and is probably caused by stress waves from the vapour explosions propagating through the melt (Ersoy, 2007). Therefore, it signifies a highly energetic, multifaceted brittle fragmentation during the water–magma interaction. It is present within ARM ash, as well as within LBAES distal tephra.

Three-dimensional multifractal properties may be related to a very high brittle deformation producing polyhedron ash or, for the same reason as put forward by Dellino and Liotino (2002), abundant ruptured vesicles increasing surface roughness. Besides, purely phreatomagmatic, blocky-equant ash gives smaller fractal dimension values than the others.

On the correlative diagrams of surface descriptors, LBAES distal tephra's intermediate character between known plinian and phreatomagmatic deposits is evident (Fig. 8). Ash <63 μm plotted on an Ra–DSA diagram shows that it is less rough, and an SA/PA diagram shows its polyhedron character. Ash surface morphology, surface descriptors, and the correlation with LBAES distal tephra's known eruptions indicate a mixed character of all types of tephra produced during the Minoan eruptive sequence.

The SA/PA ratio (3D/2D) of ash members helped to distinguish the ash of different fragmentation styles within LBAES distal ash (Fig. 9). The low SA/PA values are related to blocky, curviplanar cut ash, while high values are due to either vesiculated ash or polyhedron unvesiculated ash. SA/PA, SA/V values and a fractal dimension of roughness of <63 μm of LBAES distal tephra strongly indicate a bimodal origin, with blocky and polyhedron ash of phreatomagmatism and vesiculated ash of magmatic fragmentation. On the other hand, coarser ash (<125 μm) also exhibits phreatomagmatic affinities with an intermediate character between correlated well-known magmatic–phreatomagmatic deposits (DPD and ARM).

Our 3D volcanic ash surface morphology studies show that magmatic fragmentation processes generate different ash morphologies at different volcanic dynamics.

Tsunami interpretation

Tsunamis associated with significant explosive eruptions in marine settings are mainly generated by collapse or by the entry of pyroclastic flows (Druitt *et al.*, 2019). Because the caldera was isolated from the sea during most of the eruption, caldera collapse during the LBAES eruption could not have generated tsunamis. Nomikou *et al.* (2016) state that the tsunami waves related to LBAES were caused by the entry of pyroclastic flows generated in phases 3 and 4 into the sea. Moreover, the co-ignimbrite volcanic ash could have been generated by explosions where ignimbrite entered the sea (Walker, 1979; Freundt; 2003; Bougouin *et al.*, 2020).

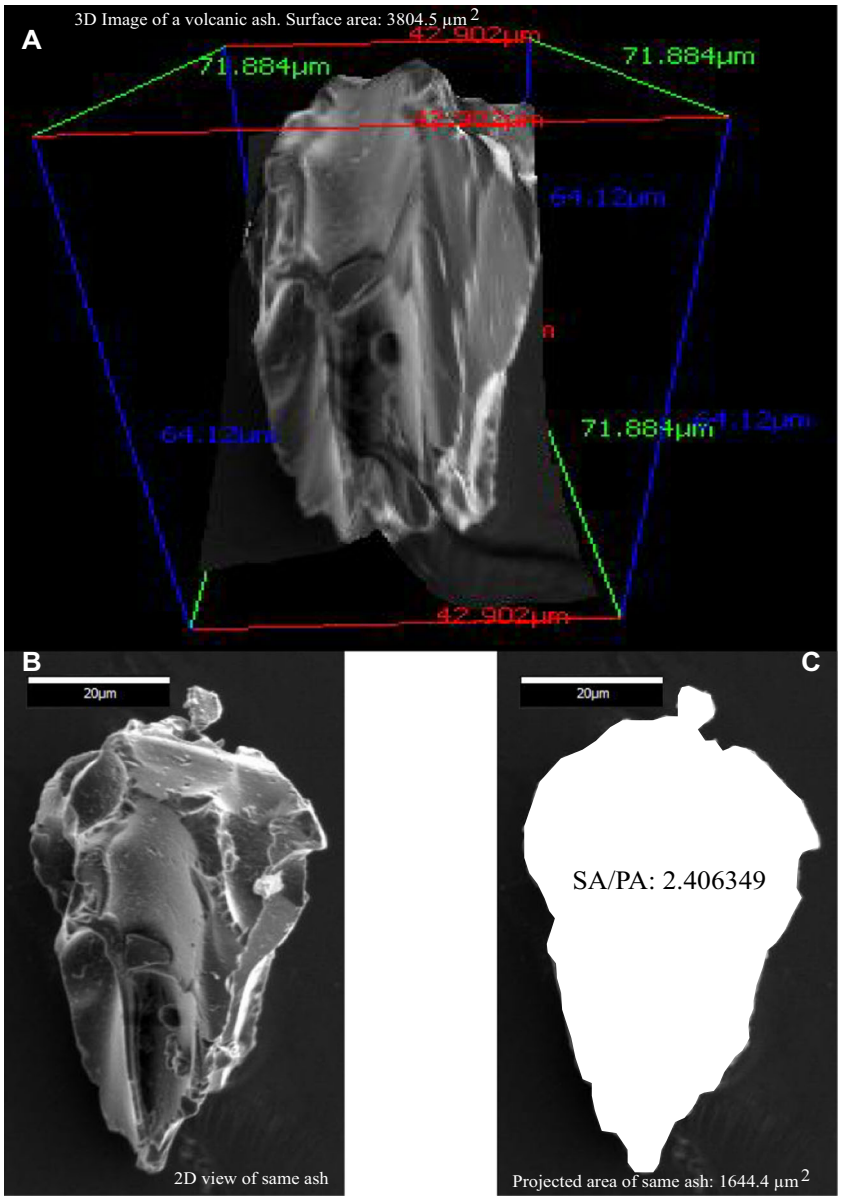

Figure 9. Illustration of 3D ash morphology and its surface area with 2D view of the same ash and its projected area. [Color figure can be viewed at wileyonlinelibrary.com].

The tsunami deposits were first described by Minoura *et al.* (2000) in the Didim and Fethiye regions in southwestern Turkey. The authors observed that the fine carbonate sand layer was underlain by 10–15 cm thick yellowish-white tephra. They also noted the lack of an erosional contact between tephra and the underlying sand layer, attributing to subsequent deposition of tephra on tsunami-related marine materials.

The relationships between tsunami deposits associated with the LBAES sequence and the tephra deposits are rarely and poorly documented in the literature. Our new ^{14}C age (3295 ± 30 BP) performed on organic material belonging to a tsunamite sequence closely matches LBAES-related tsunami deposits at Palaikastro (Crete) that yielded (uncalibrated) ^{14}C ages of 3350 ± 25 BP (Bruins *et al.*, 2009).

The overall interpretation of the sediments in the studied core and the correlation with other drilling sites (Öner, 1996, 2019; Écochard *et al.*, 2009) indicate the tsunami's volcanic origin. We speculate that marsh/lagoonal conditions prevailed at the drilling site. Öner (2019) also interpreted the preservation of the pumice layer in its *in situ* facies with the presence of the quiet environmental dynamics represented by a swamp or lagoon near Letoon. The tsunami associated with LBAES hit the study area within 30–45 min (Goodman-Tchernov *et al.*, 2009: Fig. 1) to 2.5 h (Eastwood *et al.*, 2002). The ash was deposited exclusively on top of the tsunamites, which is expected, as air travel is slower than tsunami waves. This reversal was also sketched in stratigraphical sections in Minoura *et al.* (2000). The reverse stratigraphy of these two co-origin deposits can be considered as evidence that the tsunami was formed during the eruption.

Öner (1996) used the tephra as a key horizon in some of his 25 drillings along the Eşençay River with a relatively constant thickness of *c.* 10 cm. Coastal/nearshore-originated sand was deposited by at least two consecutive tsunami waves (run-ups), giving rise to deposition of these two similar but separate sand bodies over the lagoonal mudstones in the area. It is also possible that a backwash current (return flow) after the second wave deposited this organic-rich upper layer; a phenomenon that has already been reported from several returning tsunami wave deposits (Paris *et al.*, 2007). After the ash layer's instantaneous deposition in the Eşençay Delta, mud continued to deposit, first mixed with some volcanic glass shards because of the currents. Later, it gradually passed to a quiet and anoxic marsh environment.

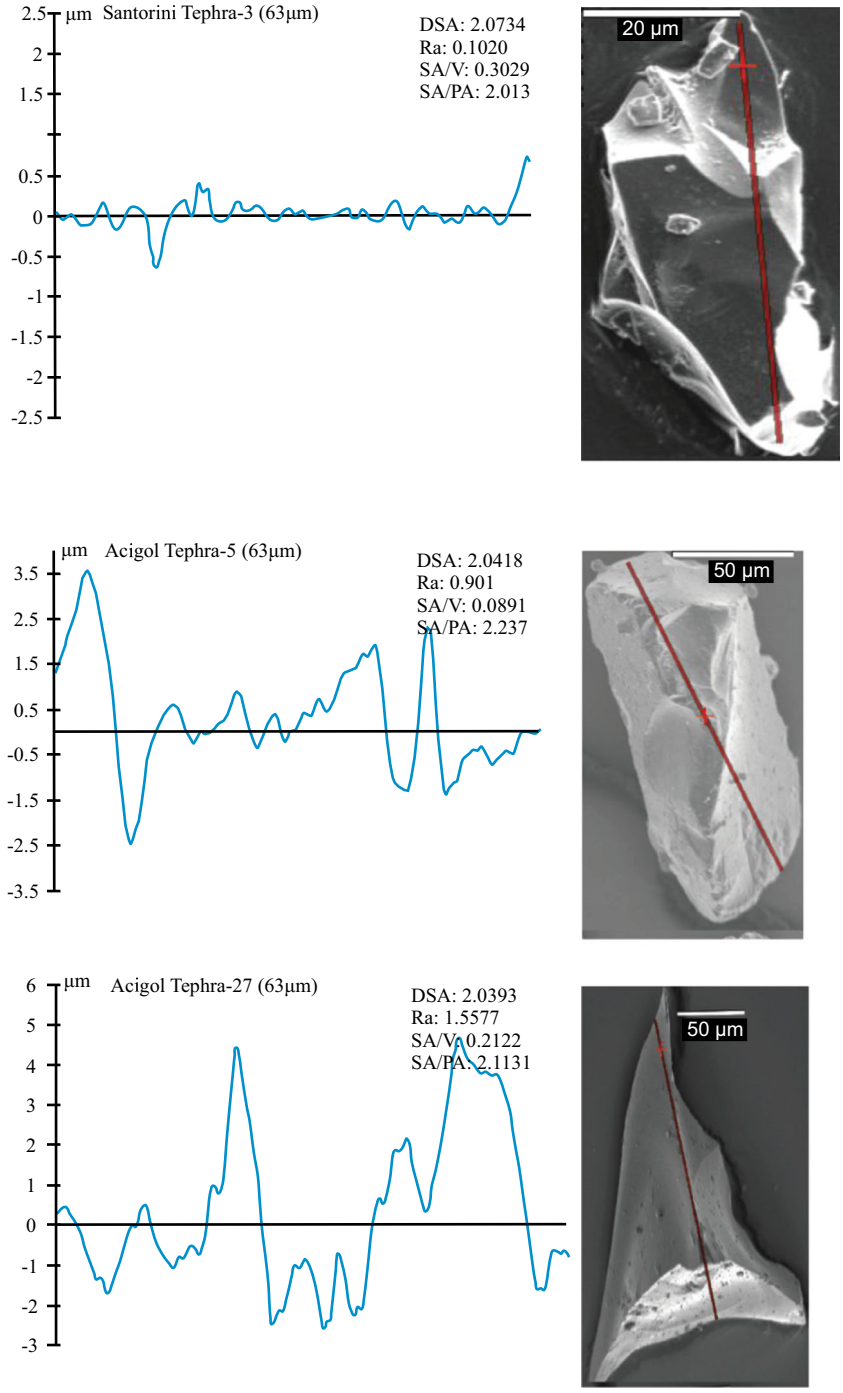

Figure 10. Polyhedron ash from different eruptions. DSA: fractal dimension of the profile; Ra: average roughness of profile; SA: surface area; PA: projected area; V: volume. [Color figure can be viewed at wileyonlinelibrary.com].

Conclusions

We examined the volcanic ash and tsunami record of the Minoan LBAES in a distal setting in southwestern Turkey. A core obtained from the Letoon Hellenic antique site in the Eşençay Delta contains a 4 cm thick tephra deposit underlain by 46 cm thick tsunami-deposited sand (tsunamite) and an organic-rich layer that we ^{14}C dated to 3295 ± 30 BP or 1633 BC. Coastal/nearshore-originated sands were carried out by at least two consecutive tsunami waves (run-ups), giving rise to the deposition of these two similar but separate sand bodies over the lagoonal mudstones in the area. The stratigraphic reversal (volcanic ash–tsunamite) indicates that ash transport time within the atmosphere took longer than tsunami propagation.

Distal LBAES tephra provides an opportunity to demonstrate the importance of the ash's textural and morphological properties to recognise the fragmentation style and thus the eruption style. It also allows the style of eruptive phase to be identified that produced distal ash. Our 3D ash morphology work advanced our understanding of the eruption and transport processes based on distal deposits.

The presence of polyhedron ash, SA/PA values and DSA-3D fractal dimension of surface roughness values shows that two distinct fragmentation mechanisms produced our single tephra layer.

The volcanic plumes generated during LBAES were under the influence of westerly winds, which diverted the ash toward the

east-southeast-northeast (McCoy and Heiken, 2000). Because of the finer grain sizes and high eruption rates, co-ignimbrite plumes cover large areas, as proposed by Sparks and Huang (1980). The LBAES-related tephra products found around the Mediterranean were not the product of a single eruptive cloud but were produced by plumes with different dynamics (plinian, phreatomagmatic and co-ignimbrite) throughout the sequence.

Based on the textural features, grain-size distribution and components (glass shards and crystals) of LBAES distal ash, we suggest that the tephra produced during the eruptive sequence (from first to the fourth phases) were injected into the atmosphere in a very short time interval, allowing a mixture in the air (plinian coarse tephra, co-ignimbrite fine tephra and phreatomagmatic tephra), during their travel towards distal regions where they have successively been deposited as a single layer.

Acknowledgements. This work was carried out within the framework of French–Turkish Cooperation. Samples collected are obtained from E. Écochard's PhD thesis, defended in 2012. We are indebted to RSJ Sparks, who critiqued an earlier draft and enriched the manuscript before submission. We thank Dr Martin Jutzeler and an anonymous reviewer for their constructive critiques that improved the paper's quality.

Data availability statement

The data that support the findings of this study are available in the supporting information.

Supporting information

Additional supporting information can be found in the online version of this article.

S1. 3D volcanic ash illustrations and their calculated surface parameters

S2. Table for calculated whole statistical parameters

References

Abbot PM, Jensen BJL, Lowe DJ *et al*. 2020. Crossing new frontiers: extending tephrochronology as a global geoscientific research tool. *Journal of Quaternary Science* **35/1-2**: 1–8.

Aksu AE, Jenner G, Hiscott RN *et al*. 2008. Occurrence, stratigraphy and geochemistry of Late Quaternary tephra layers in the Aegean Sea and the Marmara Sea. *Marine Geology* **252/3–4**: 174–192.

Athanassas CD, Modis K, Alçiçek MC *et al*. 2017. Contouring the Cataclysm: A Geographical Analysis of the Effects of the Minoan Eruption of the Santorini Volcano. *Environmental Archaeology* **23/2**: 160–176.

Bonadonna C, Ernst GGJ, Sparks RSJ. 1998. Thickness variations and volume estimates of tephra fall deposits: importance of particle Reynolds number. *Journal of Volcanology and Geothermal Research* **81**: 173–187.

Bond A, Sparks RSJ. 1976. The Minoan eruption of Santorini, Greece. *Journal of Geological Society of London*, **32**: 1–16.

Bougouin A, Paris R, Roche O. 2020. Impact of Fluidized Granular Flows into Water: Implications for Tsunamis Generated by Pyroclastic Flows. *Journal of Geophysical Research-Solid Earth* **125**: e2019JB018954.

Bruins HJ, Van der Plicht J, MacGillivray JA. 2009. The Minoan Santorini eruption and Tsunami deposits in Palaikastro (Crete): Dating by geology, archaeology, ^{14}C and Egyptian chronology. *Radiocarbon* **51**: 397–411.

Büttner R, Dellino P, La Volpe L *et al*. 2002. Thermohydraulic explosions in phreatomagmatic eruptions as evidenced by comparison between pyroclasts and products from Molten Fuel Coolant Interaction experiments. *Journal of Geophysical Research* **107**: 2277.

Cioni R, D'Oriano C, Bertagnini A. 2008. Fingerprinting ash deposits of small-scale eruptions by their physical and textural features. *Journal of Volcanology and Geothermal Research* **177**: 277–287.

Cullen VL, Smith VC, Arz HW. 2014. The detailed tephrostratigraphy of a core from the south-east Black Sea spanning the last ~60 ka. *Journal of Quaternary Science*, **29**(7), 675–690.

Dawson A, Steward I. 2007. Tsunami deposits in the geological record. *Sedimentary Geology* **200**: 166–183.

Dellino P, La Volpe L. 1996. Image processing analysis in reconstructing fragmentation and transportation mechanisms of pyroclastic deposits. The case of Monte Pilato-Rocche Rosse eruptions, Lipari (Aeolian Islands, Italy). *Journal of Volcanology and Geothermal Research*, **71**:13–29.

Dellino P, Liotino G. 2002. The fractal and multifractal dimension of volcanic ash particles contour: a test study on the utility and volcanological relevance. *Journal of Volcanology and Geothermal Research* **113**: 1–18.

Druitt T. H. 2014. New insights into the initiation and venting of the Bronze-Age eruption of Santorini (Greece), from component analysis. *Bulletin of Volcanology*, **76**(2). http://doi.org/10.1007/s00445-014-0794-x

Druitt TH, Edwards L, Mellors R *et al*. 1999. Santorini volcano, *Geological Society London Memoirs*. **19**: 165.

Druitt TH, McCoy FW, Vougioukalakis GE. 2019. The Late Bronze Age Eruption of Santorini Volcano and Its Impact on the Ancient Mediterranean World. *Elements* **15**: 185–190.

Eastwood WJ, Pearce NJG, Westgate JA *et al*. 1999. Geochemistry of Santorini Tephra in lake sediments from Southwest Turkey. *Global and Planetary Change* **21**: 17–29.

Eastwood WJ, Tibby J, Roberts N *et al*. 2002. The environmental impact of the Minoan eruption of Santorini (Thera): statistical analysis of palaeoecological data from Gölhisar, southwest Turkey. *The Holocene* **12**: 431–444.

Écochard E, Fouache E, Kuzucuoğlu C *et al*. 2009. Reconstitution paléogéographique des dynamiques paysagères durant l'Holocène autour de Xanthos et Létôon dans l'ancienne Lycie (Turquie): Premier résultats. *NOROIS (Presses Universitaires de Rennes)* **113/4**: 59–71.

Engwell SL, Sparks RSJ, Carey S. 2014. Physical characteristics of tephra layers in the deep sea realm: the Campanian Ignimbrite eruption. In *Marine Tephrochronology*, Austin WEN, Abbott PM, Davies SM, (eds). *Geological Society, London, Special Publications* **398**: 47–64.

Ersoy O. 2007. *Analyse morphologique quantitative des cendres des dépôts pyroclastiques d'origine hydrovolcanique et magmatique*. PhD thesis: Université Blaise Pascal, France.

Ersoy O. 2010. Surface area and volume measurements of volcanic ash particles by SEM stereoscopic imaging. *Journal of Volcanology and Geothermal Research* **190/3–4**: 290–296.

Ersoy O, Chinga G, Aydar E *et al*. 2006. Texture discrimination of volcanic ash from different fragmentation mechanisms: A case study, Mount Nemrut stratovolcano, eastern Turkey. *Computer and Geosciences* **32**: 936–946.

Ersoy O, Aydar E, Şen E *et al*. 2019. Contrasting fragmentation and transportation Dynamics during the emplacement of Dikkartın rhyodacitic dome; Erciyes stratovolcano, central Turkey. *Mediterranean Geoscience Reviews* **1/2**: 223–242.

Freundt A. 2003. Entrance of hot pyroclastic flows into the sea: experimental observations. *Bulletin of Volcanology* **65**: 144–164.

Friedrich WL. 2013. The Minoan Eruption of Santorini around 1613 B.C. and its consequences. In *Cultural Change in the Shadow of the Thera-Eruption? Fourth Archaeological Conference of Central Germany, October 14–16, 2011 in Halle (Saale,)* Meller H, Bertemes F, Bork H-R, et al. (eds). pp. 37–48.

Friedrich WL, Kromer B, Friedrich M *et al*. 2006. Santorini eruption radiocarbon dated to 1627-1600 B.C. *Science* **312**: 548.

Friedrichs B, Schindlbeck-Belo JC, Danisík M *et al*. 2020. New insights into source and dispersal of Mediterranean S1 tephra, an early Holocene marker horizon erupted at Mt. Erciyes (Turkey). *Quaternary Science Reviews* **249**: 106606.

Goodman-Tchernov BN, Dey HW, Reinhardt EG *et al*. 2009. Tsunami waves generated by the Santorini eruption reached Eastern Mediterranean shores. *Geology* **37**: 943–946.

Guichard F, Carey S, Arthur MA *et al*. 1993. Tephra from the Minoan eruption of Santorini in sediments of the Black Sea. *Nature* **363**: 610–612.

Hamann Y, Bowen SW, Ersoy O *et al*. 2010. First evidence of a distal early Holocene ash layer in Eastern Mediterranean deep-sea sediments derived from the Anatolian volcanic province. *Quaternary Research* **73**: 497–506.

Heiken G, McCoy F. 1984. Caldera development during the Minoan eruption, Thira, Cyclades, Greece. *Journal of Geophysical Research* **89**: 8441–8462.

Heiken G, Wohletz KH. 1985. *Volcanic Ash* University of California Press: Berkeley.

Johnston EN, Phillips JC, Bonadonna C *et al*. 2012. Reconstructing the tephra dispersal pattern from the Bronze Age eruption of Santorini using an advection–diffusion model. *Bulletin of Volcanology* **74**: 1485–1507.

Johnston EN, Sparks RSJ, Phillips JC *et al*. 2014. Revised estimates for the volume of the Late Bronze Age Minoan eruption, Santorini, Greece. *Journal of the Geological Society of London* **171**: 583–590.

Klug C, Cashman KV, Bacon CR. 2002. Structure and physical characteristics of pumice from the climactic eruption of Mount Mazama (Crater Lake), Oregon. *Bulletin of Volcanology* **64**: 486–501.

Liu EJ, Cashman KV, Rust AC. 2015. Optimising shape analysis to quantify volcanic ash morphology. *GeoResJ* **8**: 14–30.

McCoy FW, Heiken G. 2000. The Late Bronze Age explosive eruption of Thera (Santorini), Greece: regional and local effects. In *Volcanic hazards and disasters in human antiquityGeological Society of America Special Paper*, McCoy FW and Heiken G (eds). **345**: 43–70.

Minoura K, Imamura F, Kuran U *et al*. 2000. Discovery of Minoan tsunami deposits. *Geology* **28**: 59–62.

Nemeth K. 2010. Volcanic glass textures, shape characteristics and compositions of phreatomagmatic rock units from the Western Hungarian monogenetic volcanic fields and their implications for magma fragmentation. *Central European Journal of Geosciences* **2**: 399–419.

Nomikou P, Druitt TH, Hübscher C *et al*. 2016. Post-eruptive flooding of Santorini caldera and implications for tsunami generation. *Nature Communications* **7**: 13332.

Nurfiani D, Bouvet, de Maisonneuve C. 2018. Furthering the investigation of eruption styles through quantitative shape analyses of volcanic ash particles. *Journal of Volcanology and Geothermal Research* **354**: 102–114.

Öner E. 1996. The Geomorphology of Eşençay River Flood Plain and Ancient Patara Port. *Aegean Geographical Journal* **9**: 89–130.

Öner E. 2019. Landscape development of The Eşen Valley and delta plain (Letoon and Patara sites). In *Landscapes and Landforms of Turkey* Kuzucuoğlu C, Kazancı N, Çiner A (eds). Springer Verlag Book Serie; 307–321.

Paris R, Lavigne F, Wassmer P *et al*. 2007. Coastal sedimentation associated with the December 26, 2004 tsunami in Lhok Nga, west Banda Aceh (Sumatra, Indonesia). *Marine Geology* **238**: 93–106.

Peters R, Jaffe B. 2010. Identification of Tsunami Deposits in the Geologic Record: Developing Criteria Using Recent Tsunami Deposits. *U.S. Geological Survey, Reston, Virginia, Open-File Report* **1239**: 39.

Polacci M, Pioli L, Rosi M. 2003. The Plinian phase of the Campanian Ignimbrite eruption (Phlegrean Fields, Italy): evidence from density measurements and textural characterization of pumice. *Bulletin of Volcanology* **65**: 418–432.

Roberts N, Eastwood WJ, Lamb HXF *et al*. 1997. Volcanism, climate change and human impact: separating cause from effect in the palaeoenvironmental record of SW Turkey. *Third World millennium BC climate change and Old-World social collapseGlobal Environmental Change*, Dalfes N, Kukla HG and Weiss H (eds). NATO ASI Series, Series 1: **49**: 409–429.

Sarıkaya MA, Çiner A, Zreda M *et al*. 2019. Chlorine degassing constrained by cosmogenic ^{36}Cl and radiocarbon dating of early Holocene rhyodacitic lava domes on Erciyes stratovolcano, central Turkey. *Journal of Volcanology and Geothermal Research* **369**: 263–275.

Satow C, Tomlinson EL, Grant KM *et al*. 2015. A new contribution to the Late Quaternary tephrostratigraphy of the Mediterranean: Aegean Sea core LC21. *Quaternary Science Reviews* **117**: 96–112.

Schmitt AK, Danisik M, Evans NJ *et al*. 2011. Acigol rhyolite field, Central Anatolia (part 1): high-resolution dating of eruption episodes and zircon growth rates. *Contributions to Mineralogy and Petrology* **162/6**: 1215–1231.

Şen E, Aydar E, Gourgaud A *et al*. 2002. Initial explosive phases during the extrusion of volcanic lava domes: example from rhyodacitic dome of Dikkartin Dag, Erciyes Stratovolcano, Central Anatolia, Turkey. *Comptes rendus de l'Académie des Sciences* **334/1**: 27–33.

Sigurdsson H, Carey S, Devine JD. 1990. Assessment of mass, dynamics, and environmental effects of the Minoan eruption of Santorini Volcano. In *Thera and the Aegean World III*, Volume Two, Earth Sciences, Hardy DA, Keller J, Galanopoulos VP, *et al*. (eds). Thera Foundation: London; 100–112.

Smith MS, Shepherd JB. 1995. Potential Cauch.-Poisson waves generated by submarine eruptions of Kick 'em Jenny Volcano. *Natural Hazards*, **11**: 75–94.

Sparks RSJ, Huang TC. 1980. The volcanological significance of deep-sea ash layers associated with ignimbrites. *Geological Magazine* **117/5**: 425–436.

Sparks RSJ, Brazier S, Huang TC *et al*. 1983. Sedimentology of the Minoan deep-sea tephra layer in the Aegean and Eastern Mediterranean. *Marine Geology* **54**: 131–167.

Stanley DJ, Sheng H. 1986. Volcanic Shards from Santorini (Upper Minoan Ash) in the Nile Delta, Egypt. *Nature* **320**: 733–735.

Sullivan DG. 1990. Minoan tephra in lake sediments in Western Turkey: dating the eruption and assessing the dispersal of the ash. In *Thera and Aegean World III*, **Three, Chronology**, Hardy DA, Renfrew AC (eds). The Thera Foundation: London; 114–119.

Sulpizio R, Alçiçek MC, Zanchetta G *et al*. 2013. Recognition of Minoan tephra in the Acıgöl basin, western Turkey: implications for inter-archive correlations and fine ash dispersal. *Journal of Quaternary Science* **28**: 329–335.

Taddeucci J, Wohletz KH. 2001. Temporal evolution of the Minoan Eruption (Santorini, Greece), as recorded by its Plinian fall deposit and interlayered ash flow beds. *Journal of Volcanology and Geothermal Research* **109**: 299–317.

Tomlinson EL, Smith VC, Albert PG *et al*. 2015. The major and trace element glass compositions of the productive Mediterranean volcanic sources: Tools for correlating distal tephra layers in and around Europe. *Quaternary Science Reviews* **118**: 48–66.

Walker GPL. 1979. A volcanic ash generated by explosions where ignimbrite entered the sea. *Nature* **281**: 642–646.

Wohletz KH. 1983. Mechanisms of hydrovolcanic pyroclast formation: size, scanning electron microscopy, and experimental studies. *Journal of Volcanology and Geothermal Research* **17**: 31–63.

Wulf S, Kraml M, Kuhn T *et al*. 2002. Marine tephra from the Cape Riva eruption (22 ka) of Santorini in the Sea of Marmara. *Marine Geology* **183**: 131–141.